Electronic Supplementary Material (ESI) for Journal of Materials Chemistry A.
This journal is © The Royal Society of Chemistry 2014

Electronic Supplementary Material (ESI) for Journal of Materials Chemistry A.

This journal is © The Royal Society of Chemistry 2014

Facile Preparation of N- and O- Doped Hollow Carbon Spheres Derived from Poly(o-phenylenediamine) for Supercapacitors

Chengqian Yuan,[a,b] **Xianhu Liu,**[a,b] **Meiye Jia,**[a] **Zhixun Luo***,[a] **and Jiannian Yao***,[a]

Received (in XXX, XXX) Xth XXXXXXXXX 20XX, Accepted Xth XXXXXXXXX 20XX
DOI: 10.1039/b000000x

[a] *Beijing National Laboratory for Molecular Sciences (BNLMS), CAS Key Laboratory of Photochemistry, State Key Laboratory for Structural Chemistry of Unstable and Stable Species, Institute of Chemistry, Chinese Academy of Sciences, Beijing 100190, P. R. China.*
Fax: +86-10-62553453; Tel: +86-10-62553453;
E-mail: zxluo@iccas.ac.cn, jnyao@iccas.ac.cn.
[b]*University of Chinese Academy of Sciences (UCAS), Beijing 100049, P. R. China.*

S1 Morphology characterization

Fig. S1 presents SEM images of the PoPD submicrospheres synthesized at 60℃ in the absence and presence of the dopant acid, as well as the influences of monomer concentrations. A comparison analysis of Fig. S1a with 1b suggests that PoPD submicrospheres doped with glycine display a relatively unifrom size distribution than those without using the dopant.

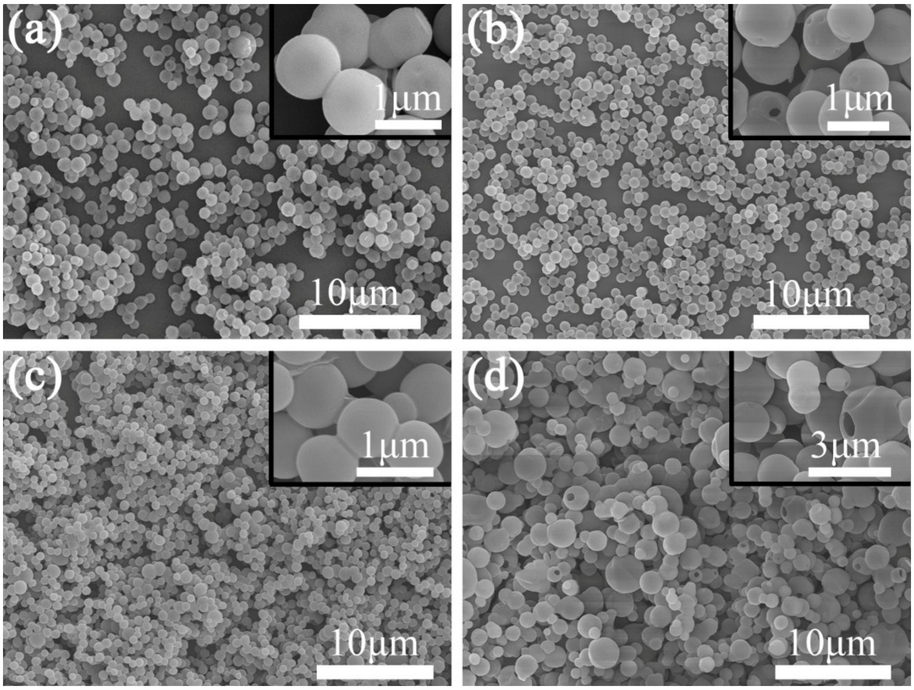

Fig. S1 SEM characterization of the PoPD submicrospheres synthesized at 60℃with influences of dopant acid and monomer concentrations: **(a)** [oPD]=0.2 M, without glycine; **(b)** [oPD]=0.2 M, with glycine; **(c)** [oPD]=0.1 M, with glycine; **(d)** [oPD]=0.4 M, with glycine.

As for the role of monomer concentrations, it was found that, when the concentration of oPD is relatively low (e.g., 0.1 M) or high (e.g., 0.4 M), both the particle sizes display a wide-range distribution (Fig. S1c and d), which is in sharp contrast with the nearly monodispersion of hollow submicrospheres (Fig. S1b) obtained at a moderate concentration [oPD]=0.2 M. This is because the stability of oPD/glycine salt micelles, as a crucial factor to control the morphology of PoPD, can be significantly influenced by the dopant and monomer concentrations.

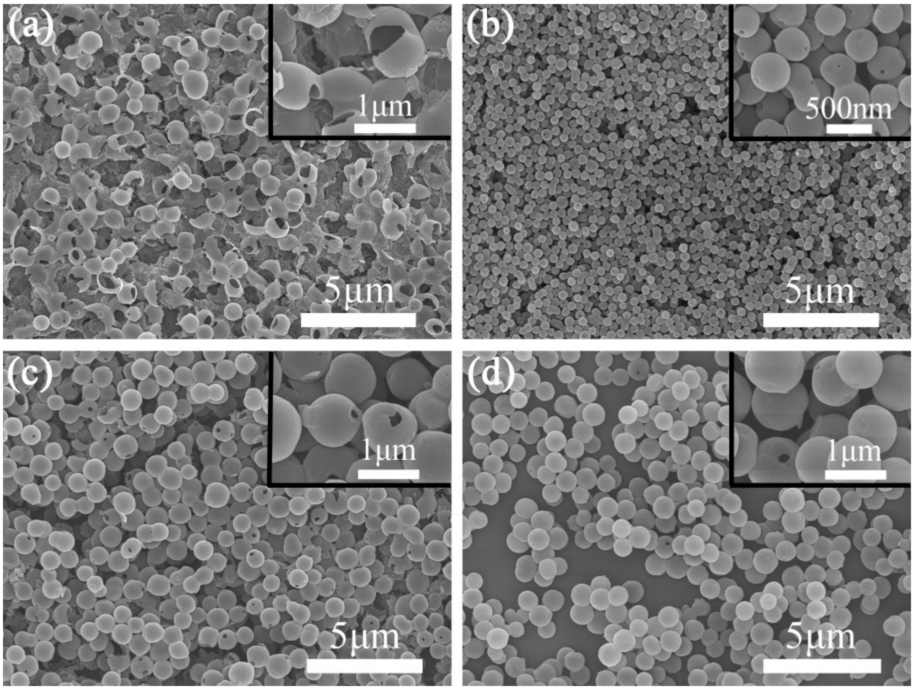

Fig. S2 SEM images of PoPD submicrospheres synthesized at different ratios of [APS]/[oPD]. **(a)** 0.5; **(b)** 1.0; **(c)** 2.0; **(d)** 3.0; other condition: [oPD]/[Gly]=1:2.

In addition, the molar ratio of oxidant to monomer is also a determining role to attain desirable PoPD submicrospheres. As clearly seen in Fig. S2, in the case of [APS]/[oPD]=0.5 only broken spheres were produced, indicating too low ratio is unfavourable for the formation of PoPD submicrospheres. With the ratio increasing to 1.0 (fused spheres with irregular holes on their surfaces), 2.0 (relatively-uniform adhering spheres) and until 3.0, the morphology changes to well-dispersed regular submicrospheres. Therefore, the polymerization rate is also an important factor to control the PoPD morophology.

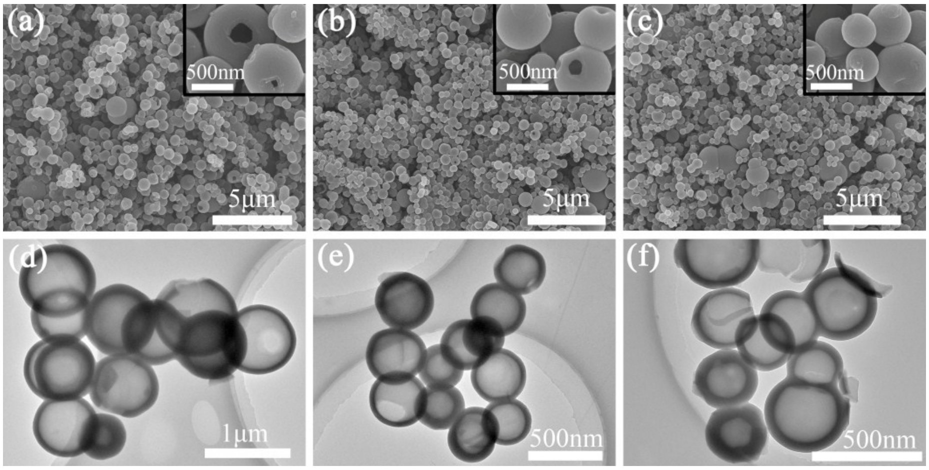

Fig. S3 SEM and TEM images of hollow carbon spheres synthesized at different carbonization temperatures. **(a/d)** 600°C; **(b/e)** 700°C; **(c/f)** 800°C.

Fig. S3 presents the representative SEM and TEM images of the N- and O-doped HCSs obtained at different carbonization temperatures. It can be seen that the carbonized products remain spherical structures as the precursor PoPD and display rare differences except for minor shrinkage with the carbonization temperatures.

S2 Structural Information

PoPD can be present in one of three oxidation states: leucoemeradine, emeraldine, and pernigraniline corresponding to reduced, reduced/oxidized and oxidized states respectively. The particular form of PoPD can be characterized by XPS by way of three different nitrogen environments with specific N1s binding energies: <399, 399-400 and >400 eV representing –N=, -NH- and -N$^{\cdot+}$- respectively. Evaluation of the N1s peak from the XPS pattern, as shown in Fig. S4 indicates that PoPD hollow submicrospheres is in the emeraldine salt form (conductive).

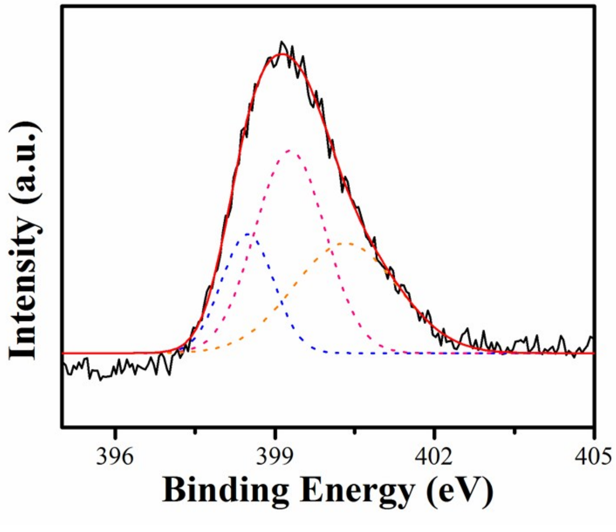

Fig. S4 High-resolution XPS spectra of N1s deconvoluted peaks of PoPD hollow submicrospheres.

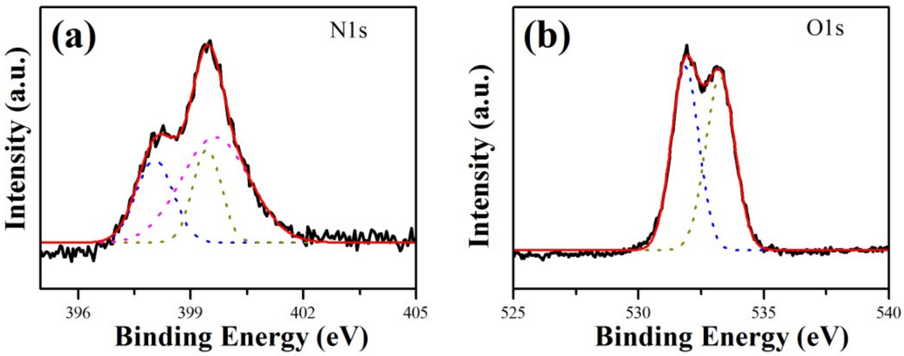

Fig. S5 High-resolution XPS spectra of N1s **(a)** and O1s **(b)** deconvoluted peaks of HCSs-600.

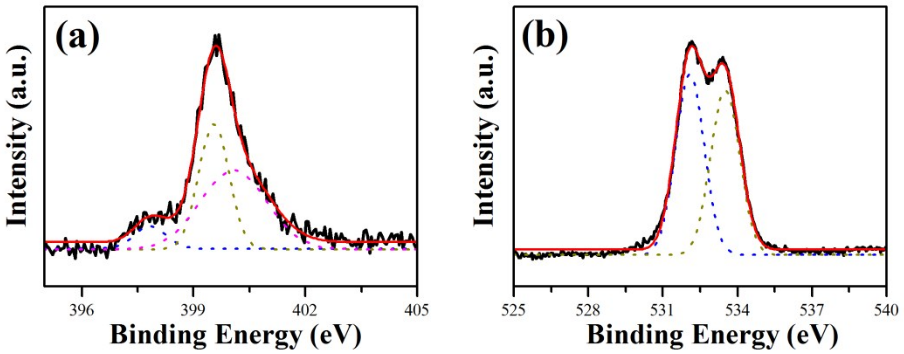

Fig. S6 High-resolution XPS spectra of N1s **(a)** and O1s **(b)** deconvoluted peaks of HCSs-800.

As displayed in Fig. S5 and S6, the N1s and O1s peaks of HCSs-600, HCSs-800 were similarly deconvoluted into peaks corresponding to N-5, N-6, N-Q; O-II, O-III respectively. However, the relative species content in different chemical state varied with the different carbonization temperatures.

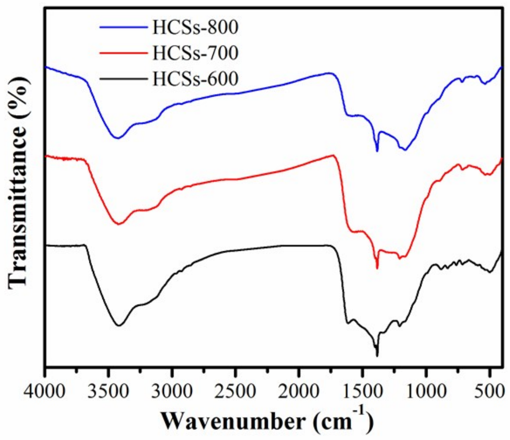

Fig. S7 FT-IR spectra of hollow carbon spheres synthesized at different carbonization temperatures.

Fig. S7 illustrates that the 1379 and 1207 cm^{-1} modes corresponding to the C−N bond display increased intensity with the elevated temperature, while 1621 cm^{-1} mode assigned to C=N becomes weakened indicating that the C=N bond could be changed to a C−N bond at the high-temperature carbonization process.

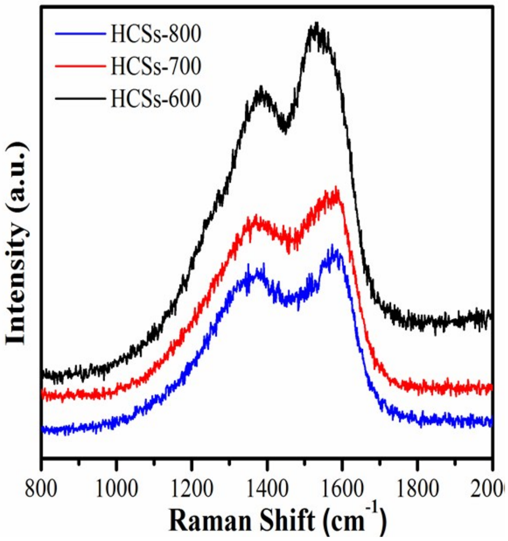

Fig. S8 Raman spectra of hollow carbon spheres synthesized at different carbonization temperatures.

Fig. S8 displays the Raman spectra of HCSs obtained at different carbonization temperatures. The intensity ratio of D-band (~1382 cm^{-1}) to G-band (~1576 cm^{-1}) reflects the graphitization degree of the carbon materials. The values of I_D/I_G for HCSs-600, HCSs-700, and HCSs-800 are 0.84, 0.87, and 0.88, respectively, indicating the graphitic degree of the carbon materials decreases in the order of HCSs-800 > HCSs-700 > HCSs -600.

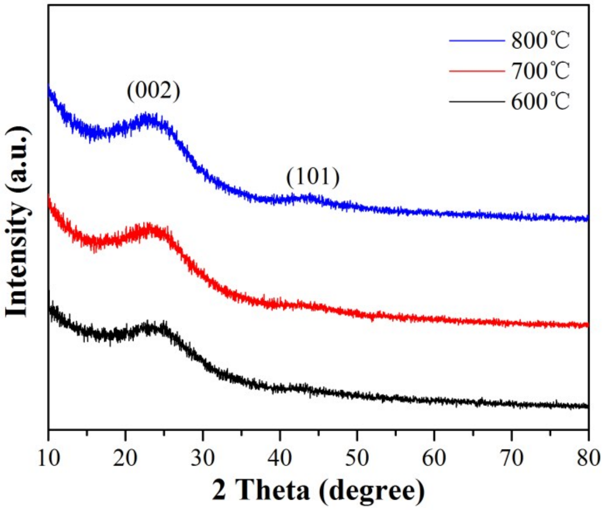

Fig. S9 XRD Patterns of hollow carbon spheres synthesized at different carbonization temperatures.

Fig. S9 depicts that, with the carbonization temperature increased from 600°C to 800°C, the intensity of (002) and (101) characteristic peaks for graphitic carbon slightly increased, suggesting the elevated degree of graphitization.

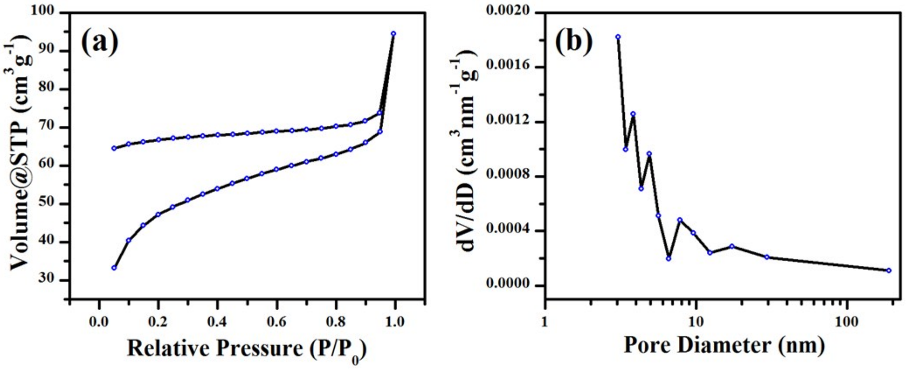

Fig. S10 (a) N_2 adsorption/desorption isotherms at 77 K and **(b)** pore size distribution of HCSs-600.

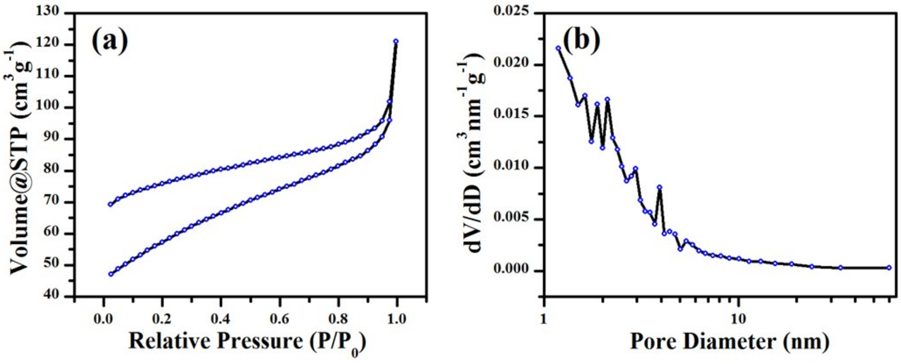

Fig. S11 (a) N_2 adsorption/desorption isotherms at 77 K and **(b)** pore size distribution of HCSs-800.

Table S1 Porous properties of hollow carbon spheres

Samples	S_{BET} (m^2g^{-1})	V_{pore} (cm^3g^{-1})	$\bar{d}_{pore}$ (nm)
HCSs-600	145	0.044	3.06
HCSs-700	355	0.14	3.83
HCSs-800	212	0.065	1.19

Fig. S10, S11 and Table S1 present the overall texture of different HCSs. It was found that HCSs-700 possesses the highest surface areas and pore volume. Besides, the decrease of surface areas and emergence of micropore in HCSs-800 are due to the collapse of pores occurred at relatively high temperature.

Fig. S12, S13 display the CV, GCD curves and the specific capacitance of HCSs-600, HCSs-800 at different current densities as supplementary materials. The profiles of CV and GCD curves of them indicate that the two samples possess both EDLC and Faradaic capacitance. Moreover, the pseudocapacitance dominates at low current densities, which is similar with that of HCSs-700.

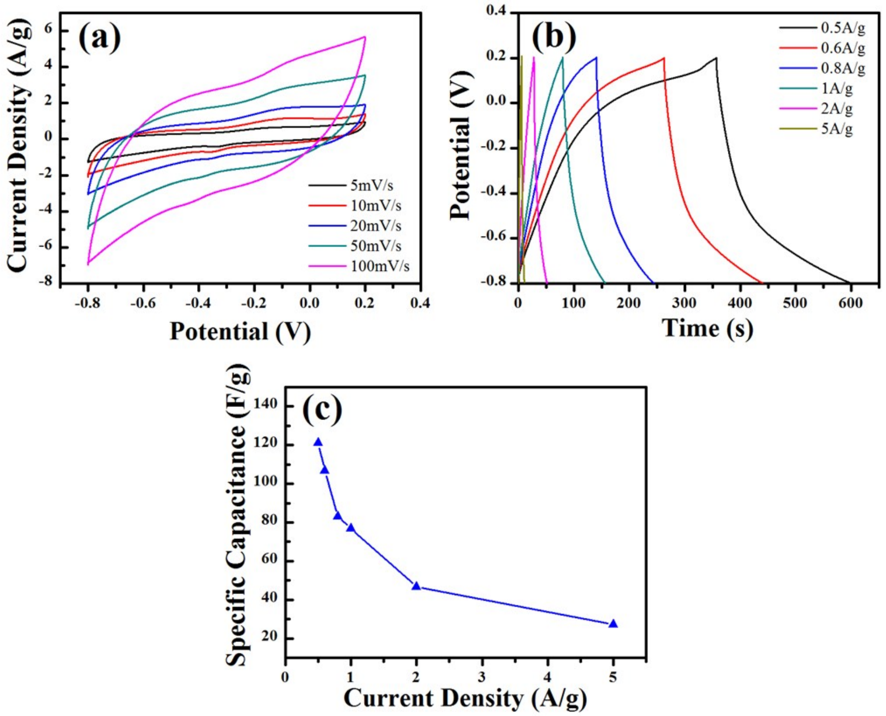

Fig. S12 (a) CVs of the HCSs-600 electrode in 6M KOH aqueous solution at different scan rates; **(b)** GCD curves of the HCSs-600 electrode at different current densities; and **(c)** A plot of the specific capacitances calculated from the discharge curves versus current density.

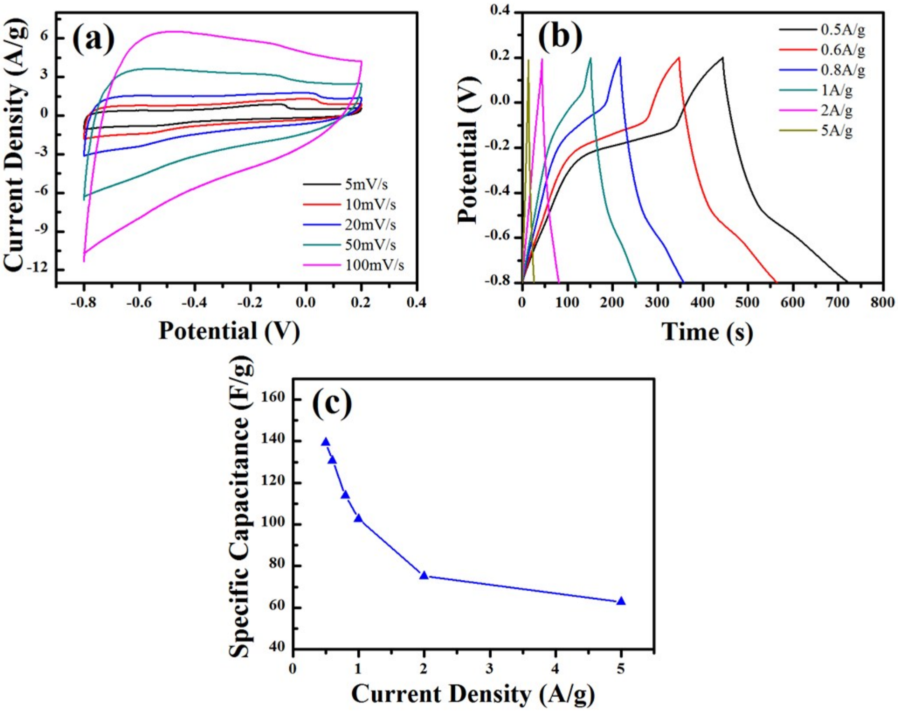

Fig. S13 (a) CVs of the HCSs-800 electrode in 6M KOH aqueous solution at different scan rates; **(b)** GCD curves of the HCSs-800 electrode at different current densities; and **(c)** A plot of the specific capacitances calculated from the discharge curves versus current density.